Check for updates

Structural phase transition drives outright photoluminescence quenching and dielectric duple bistable switching†

Zhi-Jie Wang,[a] Ming-Jing Shen, [ID][a] Zhi-Peng Rao,[a] Pei-Zhi Huang,[b] Meng-Meng Lun,[a] Bo-Wen Deng,[a] Jun-Yi Li,[a] Chang-Feng Wang, [ID][b] Hai-Feng Lu, [ID]*[b] Da-Wei Fu [ID]*[a] and Yi Zhang [ID]*[b]

Organic–inorganic metal halides (OIMHs) possessing switchable optical and electrical properties hold significant promise for applications in multifunctional sensors, switching devices, and information storage. However, the challenge lies in achieving effective regulation of optical/electric responses through structural design strategies, and materials with structural phase transition coupling photoluminescence (PL) quenching are also relatively rare. Here, by employing halogen engineering to modify the parent compound (TEMA)PbBr$_3$ (TEMA = triethylmethylammonium), we successfully obtained two derivatives (TECA) PbBr$_3$ and (TEBA)PbBr$_3$ (TECA = triethylchloromethylammonium and TEBA = triethylbromomethylammonium). Halogen engineering successfully introduces halogen–halogen interactions between PbBr$_3{}^{n-}$ inorganic frameworks and organic cations, which increases the stretching distortion of the PbBr$_6$ octahedral framework of (TECA)PbBr$_3$ and (TEBA)PbBr$_3$, accompanied by prominent orange-red broadband emission behavior in (TECA)PbBr$_3$ and (TEBA)PbBr$_3$. Meanwhile, the phase transition temperatures (T_p) of (TECA)PbBr$_3$ and (TEBA)PbBr$_3$ have also been significantly increased compared to (TEMA)PbBr$_3$, and two derivatives demonstrated switchable dielectric responses. Impressively, the reversible structural phase transition of (TECA)PbBr$_3$ and (TEBA)PbBr$_3$ dominates the outright PL quenching behavior, while still maintaining high PL emission intensity below the T_p. This represents a rare and extraordinary phenomenon in the realm of bistable responsive materials. This work provides a feasible strategy for designing and modulating photoluminescent phase transition materials and deepens understanding of the structural–performance relationship.

Introduction

Organic–inorganic metal halides (OIMHs) have shown tremendous potential for various optoelectronic applications due to their exceptional optical and electronic properties.[1–3] By assembling suitable organic amines and metal halide components, a series of novel OIMHs with optical properties has been designed and synthesized.[4–15] The photophysical properties of these OIMHs typically benefit from their highly distorted metal halide polyhedra.[16] It is worth noting that the emission of self-trapped excitons (STEs) highly correlated with lattice deformation provides inspiration for regulating OIMHs. In previous studies, a favorable lattice distortion of hybrid materials can be effectively controlled through doping engineering, which typically uses doping components such as Sb^{3+} and Mn^{2+}.[17–19] However, the regulation of structural distortion at the molecular level and the construction of optical/electric bistable switchable materials, which are highly attractive for optoelectronic device applications, need to be explored.

Organic–inorganic hybrid components are also prone to structural phase transition under thermal stimulation,[20–39] which can affect their emission intensity and even lead to a PL quenching phenomenon.[28,40] At present, many photoluminescent OIMHs exhibit PL decay during phase transitions, such as [(CH$_3$)$_3$NCH$_2$CH$_3$]$_2$MnCl$_4$,[41] (2-methylimidazolium)MnCl$_3$(H$_2$O),[42] and [(CH$_3$)$_3$PCH$_2$OCH$_3$][PbBr$_3$],[43] among others. However, the phenomenon of structural phase transition coupled with PL

[a]Ordered Matter Science Research Center, Jiangsu Key Laboratory for Science and Applications of Molecular Ferroelectrics, Southeast University, Nanjing 211189, People's Republic of China. E-mail: dawei@seu.edu.cn
[b]Institute for Science and Applications of Molecular Ferroelectrics, Key Laboratory of the Ministry of Education for Advanced Catalysis Materials, Zhejiang Normal University, Jinhua 321019, People's Republic of China.
E-mail: luhaifeng@zjnu.edu.cn, yizhang1980@seu.edu.cn

2290 | *Inorg. Chem. Front.*, 2024, **11**, 2290–2299

This journal is © the Partner Organisations 2024

quenching is exceedingly rare compared to the attenuation phenomenon of PL during structural phase transition in OIMHs. Lun *et al.* observed an unusual temporary PL quenching effect coupled with structural phase transition at 340 K in $(DMML)_2MnBr_4$ ($DMML = N,N$-dimethylmorpholinium). This phenomenon originates from the anomalous variation in the $[MnBr_4]^{2-}$ tetrahedron, causing the absorbed energy to be relaxed by non-radiative transitions.[44] Spanopoulos *et al.* synthesized a 1D (one-dimensional) lead-free halide OIMH $(DAO)Sn_2I_6$ ($DAO = 1,8$-octyldiammonium) that undergoes a structural phase transition at 415 K accompanied by PL quenching and exhibits stable PL intensity over a wide temperature range of 145–415 K.[45] Given its enormous value, there is still research potential for designing structural phase transition materials coupled with PL quenching through an effective strategy.

>What attracts us is that halogen bonding, as a typical intermolecular interaction, provides a fascinating tool in crystal engineering as it can regulate the structure and properties of materials. This occurs when there is evidence of an attractive interaction between the electrophilic region associated with halogen atoms in one molecular entity and the nucleophilic region in another or the same molecular entity.[46] This interaction acts like a pulling rope between organic cations and inorganic anionic frameworks, which is conducive to achieving effective structural distortion and phase transition regulation. Based on the above research inspiration, we have introduced

halogen–halogen interactions to $(TEMA)PbBr_3$ and obtained two 1D OIMHs single crystals, $(TECA)PbBr_3$ and $(TEBA)PbBr_3$, which exhibit broad orange-red light emission centered at 665 nm and a stable PL emission intensity of up to 393/454 K. We found that with the introduction of halogen–halogen interaction, the degree of octahedral stretching distortion of two derivatives increased, and the T_p significantly increased. Notably, $(TECA)PbBr_3$ and $(TEBA)PbBr_3$ exhibit highly coupled PL quenching and structural phase transition. This work provides a feasible strategy for the design and modulation of photoluminescent phase transition materials and opens a new window for OIMHs as optoelectronic intelligent device applications at higher operating temperatures.

Results and discussion

Structural description

Single crystals of the three compounds were prepared by the solvent evaporation method (see the Experimental section for details). Single-crystal X-ray diffraction characterized the structures of three compounds. The crystal structures of $(TEMA)PbBr_3$, $(TECA)PbBr_3$, and $(TEBA)PbBr_3$ are isostructural, adopting the 1D hexagonal ABX_3 perovskite structure, where organic cations occupy the cavities between adjacent infinite $[PbBr_3]^-$ chains (Fig. 1a and Fig. S1, S2†).
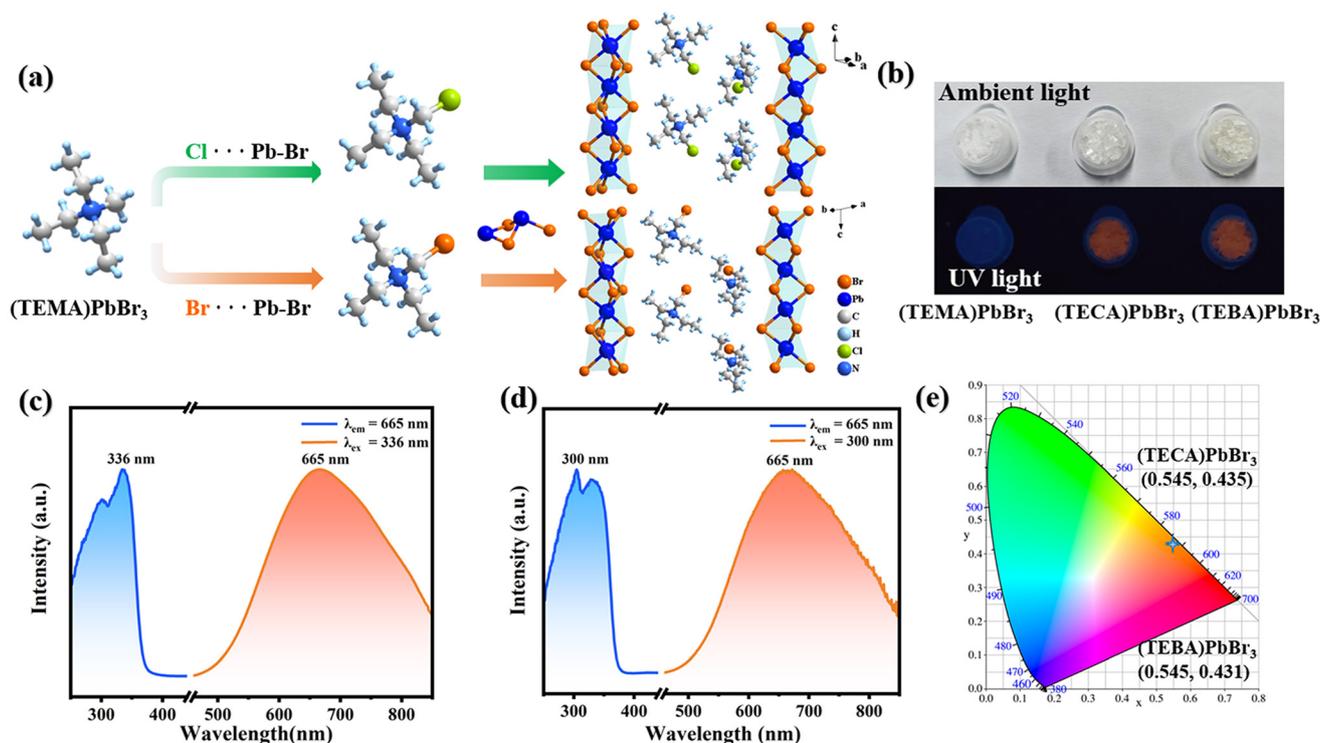
Fig. 1 (a) The molecular structure and packing structures (without hydrogen atoms) of (TEMA)PbBr₃, (TECA)PbBr₃ and (TEBA)PbBr₃. (b) Photographic of crystals under ambient light and ultraviolet light irradiation based on 254 nm at room temperature. (c) PL and PLE spectra for (TECA)PbBr₃ at room temperature. (d) PL and PLE spectra for (TEBA)PbBr₃ at room temperature. (e) CIE chromaticity coordinates of (TECA)PbBr₃ and (TEBA)PbBr₃.

Specifically, the three compounds crystallize in the $P2_1/c$ space group, exhibiting regular arrangements of organic amine cations and $[PbBr_3]^-$ skeletons. The phase purity of the target crystal sample was determined by powder X-ray diffraction (PXRD) (Fig. S3†). The chemical composition and functional group information were also investigated by infrared spectroscopy (Fig. S4†), in which the peaks at approximately 750 and 521 cm^{-1} belong to the characteristic absorption of the C–Cl bond in (TECA)PbBr$_3$ and the C–Br bond in (TECA)PbBr$_3$, respectively.

Optical properties

The UV-visible diffuse reflectance absorption spectra display distinct absorption bands in the UV region at around 350 nm for all three compounds (Fig. S5†). Meanwhile, the calculated optical bandgaps (E_g) based on the Tauc plot are determined to be 3.42 eV for (TEMA)PbBr$_3$, 3.40 eV for (TECA)PbBr$_3$, and 3.39 eV for (TEBA)PbBr$_3$, respectively (Fig. S5†). When subjected to ultraviolet light irradiation at room temperature (Fig. 1b), crystals of (TEMA)PbBr$_3$ do not exhibit apparent PL behavior. However, crystals of (TECA)PbBr$_3$ and (TEBA)PbBr$_3$ can emit orange-red light at room temperature, consistent with the orange chromaticity coordinates defined by the Commission internationale de l'éclairage (CIE) coordination (Fig. 1e). Hence, a more detailed optical investigation was conducted to explore the PL properties of (TECA)PbBr$_3$ and (TEBA)PbBr$_3$. As depicted in Fig. 1c and d, both compounds demon-

strate distinct broadband emission spectra at room temperature, with noticeable emission peaks observed at around 665 nm and a full width at half maximum (FWHM) of around 205 nm. Notably, when the emission wavelength is fixed at 665 nm, (TEBA)PbBr$_3$ showcases two adjacent absorption peaks at 300 and 320 nm, respectively, while (TECA)PbBr$_3$ exhibits two adjacent absorption peaks at 310 and 336 nm, respectively. Meanwhile, the PLQY values of the powder samples measured at 298 K are 2.78% and 2.38% (Fig. S6 and S7†), respectively. Additionally, the PL decay curve monitored at 665 nm was fitted with a theoretical double exponential function, yielding average lifetimes of 23.9 and 33.5 ns for (TECA)PbBr$_3$ and (TEBA)PbBr$_3$ (Fig. 2c), respectively.

To further investigate the relationship between the PL and temperature, temperature-dependent PL spectra were also measured (Fig. 2a and b). As the temperature increases from 303 K to 393 K for (TECA)PbBr$_3$, and the temperature increases from 303 K to 453 K for (TEBA)PbBr$_3$, both the PL emission intensities show a monotonic decreasing trend, which is because the rise in temperature endows the electrons with sufficient kinetic energy to surmount the energy barrier, thereby favoring recombination through non-radiative pathways. It is noteworthy that the emission intensity still maintains a high order of magnitude (10^4–10^5) before reaching the critical temperature point of 393/454 K. However, after reaching the critical temperature point of 393/454 K, the PL is entirely quenched (Fig. 2d and e).
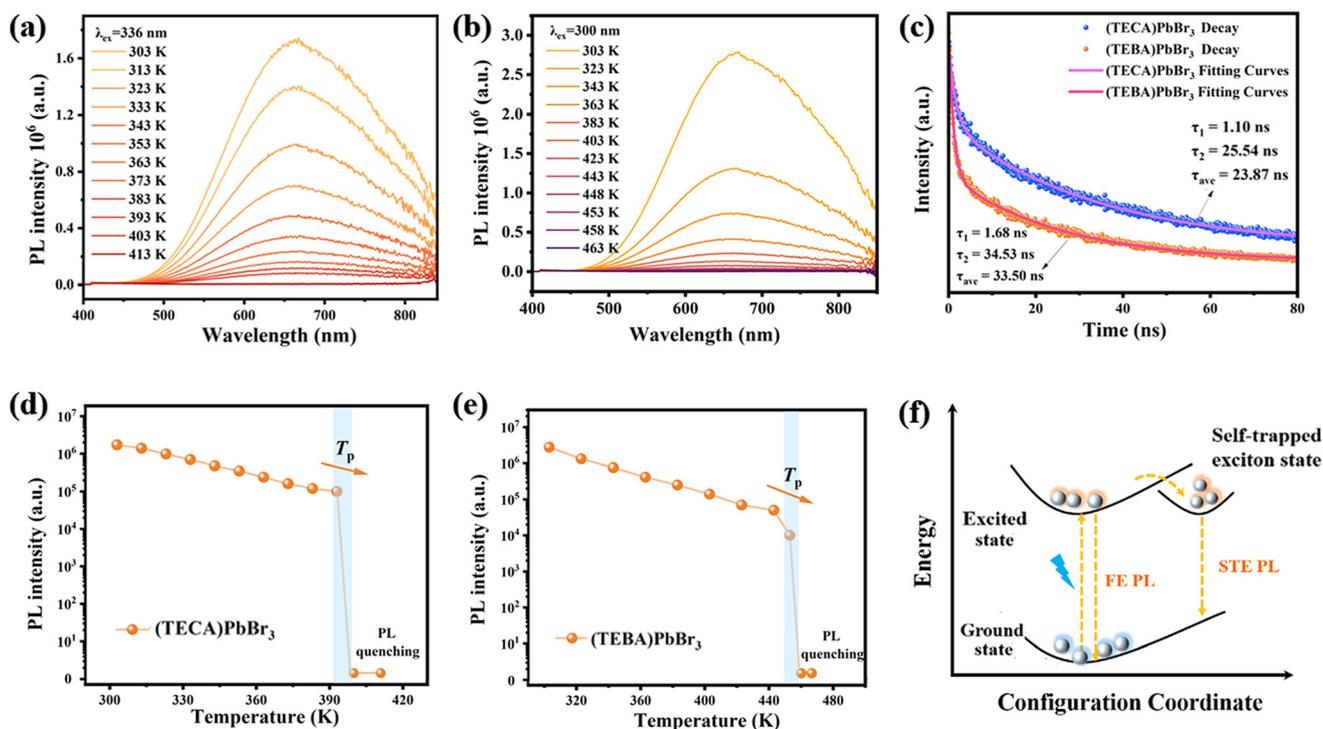
Fig. 2 (a) Temperature-dependent PL spectra of (TECA)PbBr$_3$. (b) Temperature-dependent PL spectra of (TECA)PbBr$_3$. (c) PL decay lifetime curves of (TECA)PbBr$_3$ and (TEBA)PbBr$_3$. (d) PL trend from 303 to 413 K of (TECA)PbBr$_3$. (e) PL trend from 303 to 463 K of (TEBA)PbBr$_3$. (f) Illustration of the STE mechanism for the broadband emission.

2292 | *Inorg. Chem. Front.*, 2024, **11**, 2290–2299

This journal is © the Partner Organisations 2024

Thermal properties and dielectric properties

This type of material is prone to undergoing structural phase transitions under thermal stimulation, resulting in modification of the physical properties. Differential scanning calorimetry (DSC), as a thermal analysis technique, is effectively used to analyze the phase transition. As shown in Fig. 3a, (TEMA)PbBr$_3$ exhibits obvious endothermic and exothermic peaks at 293/273 K during the entire heating/cooling cycles. By introducing halogen engineering, the T_p of OIMHs effectively achieved a remarkable enhancement of 100 K for (TECA)PbBr$_3$ and 161 K for (TEBA)PbBr$_3$ (Fig. S8†), respectively, which are also representative of high-temperature 1D lead-based phase transition materials at present (Fig. 3b). The large thermal hysteresis and sharp peaks exhibited by the three compounds indicate that they experience a first-order phase transition. For the convenience of subsequent discussions, the entire process is divided into the room temperature phase (RTP) and the high-temperature phase (HTP) when the temperature is below or above T_p, respectively. In the solid–solid phase transition, there is usually a thermally driven dielectric anomaly in the vicinity of T_p, involving the mutual switching of dielectric constants in specific materials under external stimuli. As shown in Fig. 3c, d and Fig. S8,† temperature-dependent dielectric measurements were performed on the three compounds at 1 MHz, revealing different dielectric anomaly temperatures. Specifically, the real part (ε') of the dielectric constants shows a pair of distinct step-like dielectric anomalies at approximately 293 K for (TEMA)PbBr$_3$, 393 K for (TECA)PbBr$_3$ and 454 K for (TEBA)PbBr$_3$ upon heating and cooling, which is closely aligned with the findings from the DSC results. Hence, we were pleasantly surprised to find that the PL quenching behavior is highly coupled with the structural phase transition, which is a relatively rare phenomenon. Meanwhile, the temperature range of the PL emission was also significantly expanded by introducing halogen engineering. Furthermore, as depicted in Fig. S9,† (TECA)PbBr$_3$ and (TEBA)PbBr$_3$ demonstrated excellent reversibility and fatigue resistance in switchable dielectric properties, as observed through repeated heating and cooling cycles between high and low dielectric states. Simultaneously, as presented in Fig. S10 and S11,† the thermally reversible photoluminescence quenching–activation cycles of both compounds also exhibit good reversibility around the T_p. These findings suggest that these compounds
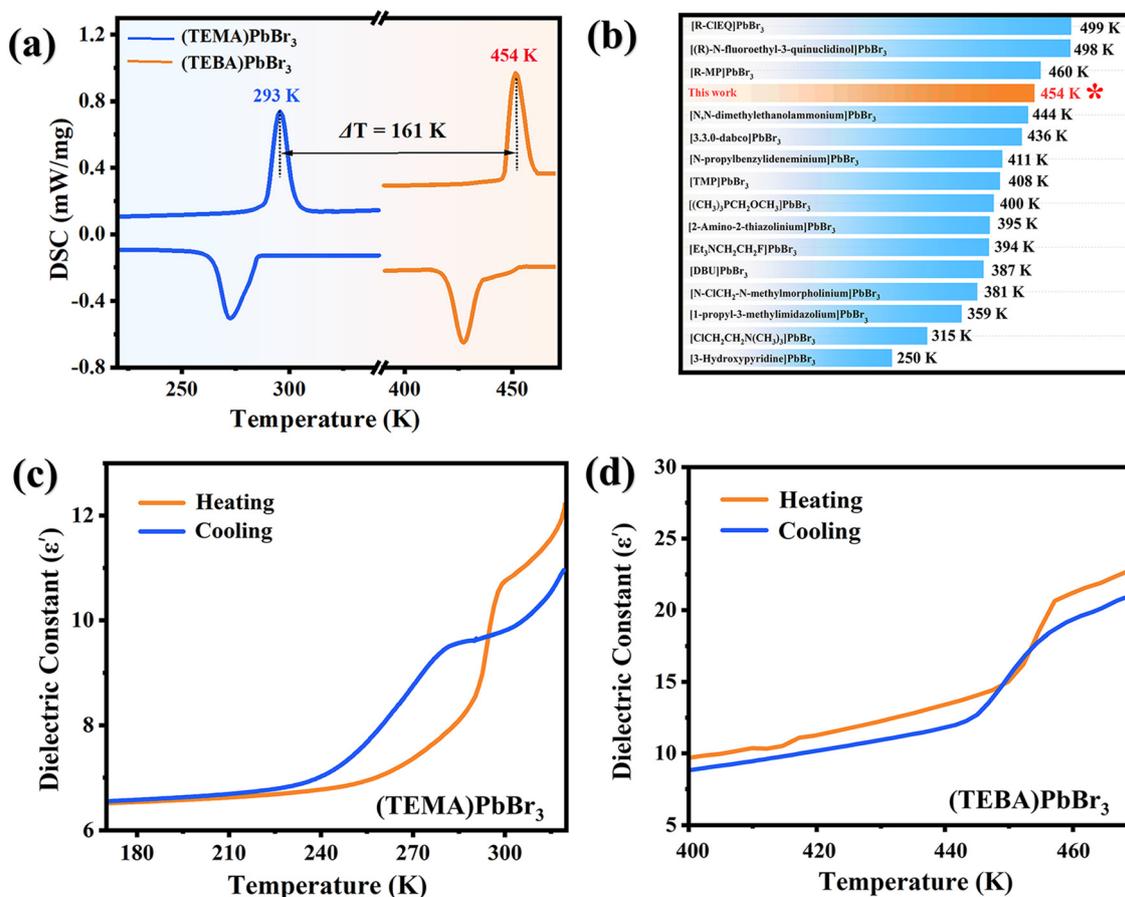
Fig. 3 (a) DSC curves of (TEMA)PbBr$_3$ and (TEBA)PbBr$_3$ in the heating–cooling cycle. (b) The currently reported 1D lead bromide perovskite phase transition temperature compared with the highest phase transition temperature in this work. The temperature-dependent real part (ε') of the complex dielectric constant of (TEMA)PbBr$_3$ (c) and (TEBA)PbBr$_3$ (d) at 1 MHz.

This journal is © the Partner Organisations 2024

Inorg. Chem. Front., 2024, **11**, 2290–2299 | **2293**

have potential as thermal responsive dielectric/photo-luminescence switching materials.

Phase transition analysis

To reveal the underlying mechanism of the above phenomenon, the compounds were characterized by variable-temperature single-crystal X-ray diffraction. As shown in Fig. S12 and S13,† after the successful implementation of halogen engineering, the halogen–halogen interactions in the structure were successfully constructed. Meanwhile, the lead halide octahedral Pb–X bond lengths and bond angles of the three compounds display corresponding alterations (Fig. 5a and Tables S4–S6†). In the HTP, both (TEMA)PbBr$_3$ and (TECA)PbBr$_3$ crystallize in the $P6_3/mmc$ space group ($6/mmc$ point group). Unlike the cation general position observed in RTP, the cation TEMA$^+$ in (TEMA)PbBr$_3$ occupies a special site of $6/mmm$ to fulfill the symmetry requirements by leveraging either a 6-fold axis orientational disorder or rotation (Fig. 4a and b). Similarly, (TECA)PbBr$_3$ also manifests this 6-fold disorder behavior.[47] Notably, the inorganic [PbBr$_3$]$^-$ skeleton exhibits negligible disorder within its structure, accompanied by homogenization of Pb–Br bond lengths (Fig. 5b). Consequently, the structural phase transition observed in (TEMA)PbBr$_3$ and (TECA)PbBr$_3$ can be attributed to an ordered–disordered transition of organic cations.

Unfortunately, due to the deterioration of crystal quality after undergoing high-temperature phase transitions, the high-temperature structure of (TEBA)PbBr$_3$ could not be determined. We conducted *in situ* temperature-dependent PXRD measurements to further verify the relevant information on the structural phase transition (Fig. S14†). It was observed that significant changes occurred in the PXRD data after the phase transition of (TEBA)PbBr$_3$, as shown in Fig. 4d. Specifically, diffraction peaks did not exhibit marked differences in their positions from 298 K up to 403 K. However, upon reaching 454 K, most of the diffraction peaks disappeared, especially diffraction peaks located at around 15°, 23°, and 25–35°. After the temperature transitions to 463 K, there is no significant difference in the pattern of diffraction peaks. Moreover, upon cooling the sample back to room temperature, the measured PXRD patterns were consistent with the patterns obtained prior to heating, providing evidence for the reversibility of the phase transition.

To further explore the impact of halogen–halogen interactions on the phase transition of the system, we utilized the OLEX2 software to calculate the void occupancy of the three compounds. In hybrid phase transition materials, there exists a discernible correlation between the void occupancy and the T_p, which can be employed to better elucidate the relationship between the strength of intermolecular forces, spatial steric hindrance, and the phase transition temperature.[48] As depicted in Fig. 4c–e, the quantitative void occupancy values are determined to be 30.07% in (TEMA)PbBr$_3$, 27.52% in (TECA)PbBr$_3$, and 27.22% in (TEBA)PbBr$_3$, aligning with the lower void occupancy and higher phase transition temperature. Therefore, with the introduction of halogen–halogen
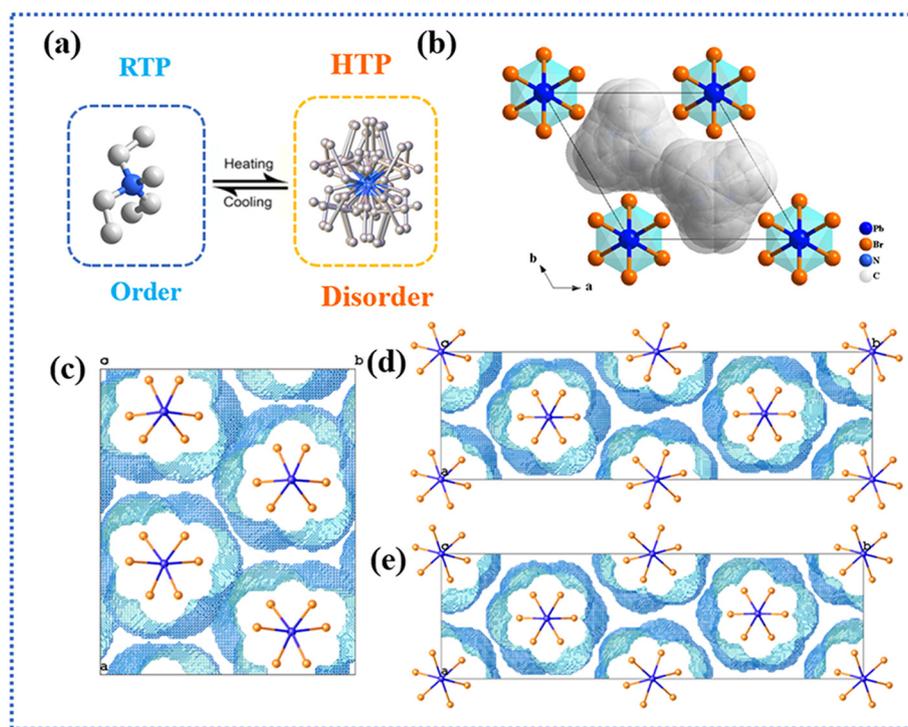
Fig. 4 (a) Order−disorder transition of organic cations [TEMA]$^+$. (b) The packing structures (without hydrogen atoms) of (TEMA)PbBr$_3$ at HTP. Void diagram between anionic frameworks in the unit cell of (TEMA)PbBr$_3$ (c), (TECA)PbBr$_3$ (d) and (TEBA)PbBr$_3$ (e).

2294 | *Inorg. Chem. Front.*, 2024, **11**, 2290–2299

This journal is © the Partner Organisations 2024
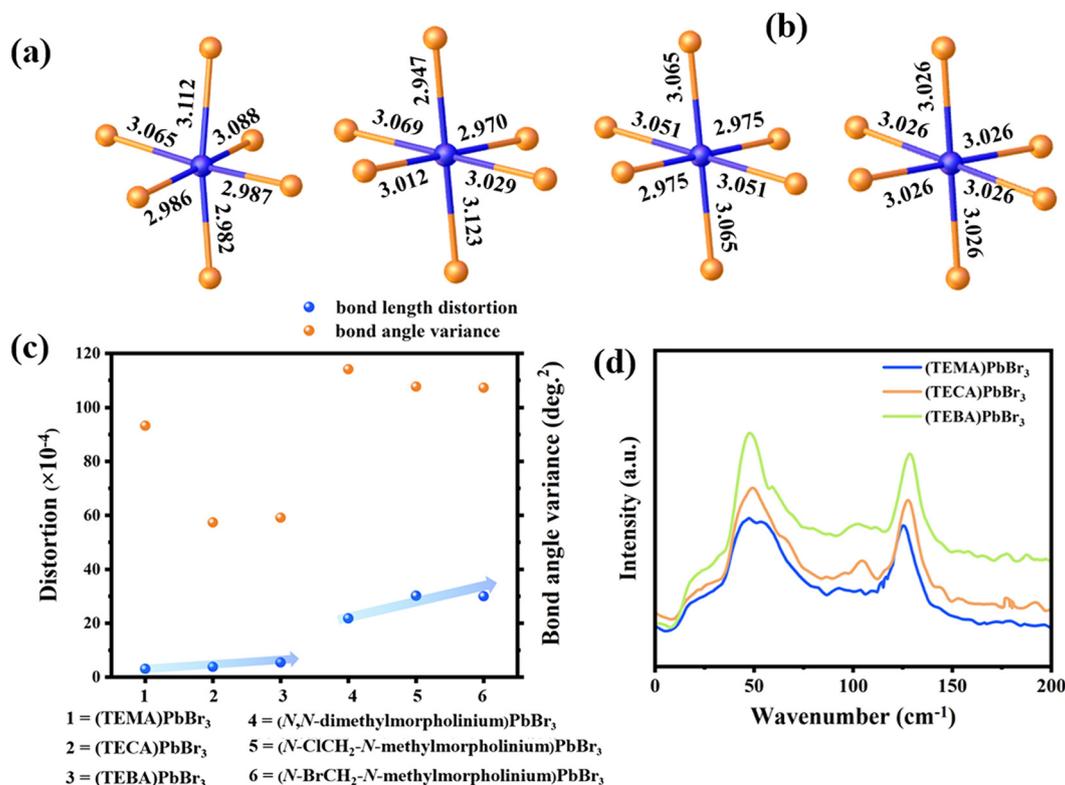
Fig. 5 (a) The octahedral units of three compounds at LTP. (b) The standard $PbBr_6$ octahedron at HTP. (c) Bond length distortion and bond angle variance of the six compounds calculated based on the crystal structures. (d) Low frequency Raman spectra of three compounds.

interactions, the phase transition behavior of the compounds is also effectively regulated.

Structural distortion and Raman spectroscopy

To further investigate the effect of halogen–halogen interactions on the $PbBr_6$ octahedral framework, the bond length distortion (Δd) and bond angle variance (σ^2) of the $PbBr_6$ octahedron were calculated based on eqn (1) and (2).[49] Here, d_i represents the independent bond lengths of Pb–Br, d_0 represents the average Pb–Br bond lengths, and θ_i represents the single bond angle of Br–Pb–Br. The quantitative values for Δd and σ^2 are determined to be 3.01×10^{-4} and 93.279 in (TEMA)$PbBr_3$, 3.82×10^{-4} and 57.283 in (TECA)$PbBr_3$, and 5.45×10^{-4} and 59.101 in (TEBA)$PbBr_3$ (Fig. 5c). For the angle distortion, octahedra typically have higher distortion values as the face-sharing connectivity of octahedra requires bending angles (i.e. Br–Pb–Br angles). It is worth noting that the introduced halogen–halogen interactions have a more significant effect on the stretching of the bond length, in which the difference in the variation of the Pb–Br bond length is found to follow the trend of (TEBA)$PbBr_3$ > (TECA)$PbBr_3$ > (TEMA)$PbBr_3$. Similarly, the trends are also observed in the 1D PL of lead bromide based on halogenated N-methylmorpholine systems,[50] as shown in Fig. 5c.

$$\Delta d = \frac{1}{6} \sum_{i=1}^{6} [(d_i - d_0)/d_0]^2 \tag{1}$$

$$\sigma^2 = \frac{1}{11} \sum_{i=1}^{12} (\theta_i - 90°)^2 \tag{2}$$

To better understand the local structural dynamics of the three compounds, low-frequency Raman measurements were conducted. Raman spectroscopy was conducted under ambient conditions using 532 nm laser excitation. As shown in Fig. 5d, the three compounds have well-resolved spectra. The peaks at lower wavenumbers (15–100 cm^{-1}) originate from the bending of Br–Pb–Br bonds, while the peaks at higher wavenumbers (100–180 cm^{-1}) originate from the stretching of Pb–Br bonds, which provides a reference for a detailed comparison of the local structural dynamics in the three compounds.[51] Fortunately, for the three 1D face-sharing lead bromide perovskites, the peak of the stretching symmetry mode of Pb–Br bonds reaches its maximum value in (TEBA)$PbBr_3$, which is highly consistent with the structural analysis of the Pb–Br bond length distortion. Similarly, the effect on exciton–phonon coupling in 1D TMAPbBr$_{3-x}I_x$ perovskites is primarily influenced by the vibration mode of the Pb–X bond stretching within the PbX_6 octahedra, rather than the mode of X–Pb–X angle bending.[52] Therefore, the introduction of halogen–halogen interactions leads to uneven Pb–Br bond lengths and more prominent distortion of the $PbBr_6$ octahedron, which is of significant consequence for the emission of self-trapped excitons. Meanwhile, the quenching of PL is related to the disappearance of this stretching distortion, and the $PbBr_6$ octa-
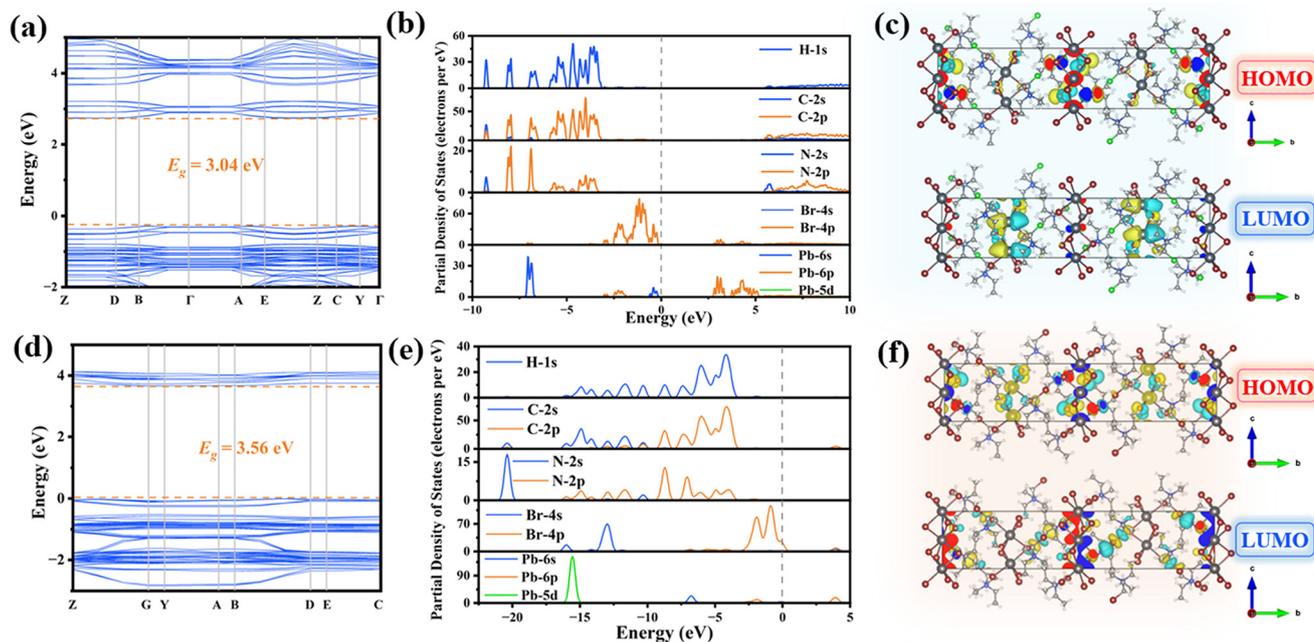
Fig. 6 The calculated band structures and PDOS of (TEMA)PbBr$_3$ (a and b) and (TEBA)PbBr$_3$ (d and e). The calculated frontier molecular orbital (FMO) diagram: HOMOs and LUMOs of (TEMA)PbBr$_3$ (c) and (TEBA)PbBr$_3$ (f).

hedron at HTP becomes more consistent with the standard octahedron (Fig. 5b).

Density functional theory (DFT) calculations

To further elucidate the broadband emission mechanism and study the band structures, density functional theory (DFT) calculations were performed. Spin–orbit coupling (SOC) was taken into account because the inclusion of the heavy atom lead (Pb) in the halides significantly influences the band structure and projected density of states (PDOS). As depicted in Fig. 6a, d and Fig. S15,† the calculated simulated band gaps are found to be 3.04 eV in (TEMA)PbBr$_3$, 3.59 eV in (TECA)PbBr$_3$, and 3.56 eV in (TEBA)PbBr$_3$, which deviate slightly from the experimentally observed optical band gaps. Also, the valence band maximum (VBM) and conduction band minimum (CBM) positions in the Brillouin zone are located at the same K-vector, indicating that the three compounds can be classified as direct bandgap semiconductors, which is also consistent with the results revealed by the sharp absorption edge in the UV-vis absorption. As depicted in the density of states and frontier orbital diagram (Fig. 6b, e and Fig. S15†), the VBM is primarily derived from the Br-4p state, while the CBM is contributed by the Pb-6p state. The frontier orbitals below and above the Fermi level are predominantly determined by the inorganic lead halide framework, with electronic states largely confined to the isolated lead halide 1D chains (Fig. 6c, f and Fig. S16†). Consequently, electron transfer and PL emission mainly occur within the inorganic frameworks. Combined with the optical experiment results, the broadband emission of the

two compounds arises from STE emission, as illustrated in Fig. 2f. This phenomenon can be attributed to the strong electron–phonon coupling occurring within deformable lattices and this PL mechanism has been corroborated in numerous low-dimensional OIMHs.[16,50,51]

Conclusions

In summary, we have successfully demonstrated the effectiveness of halogen–halogen interactions as a directional structural design strategy for the rational regulation of the optical/dielectric response of OIMHs. By introducing halogen–halogen interactions, the Pb–Br bond stretching distortion of the three compounds gradually intensifies, effectively eliciting STE broadband emissions in (TECA)PbBr$_3$ and (TEBA)PbBr$_3$, which arise from the introduction of controlled distortions in the inorganic framework and prove to be highly beneficial for facilitating the formation of self-trapped excitons, thus holding immense significance in the generation of broadband emissions. Meanwhile, halogen–halogen interactions regulate the T_p and enable (TECA)PbBr$_3$ and (TEBA)PbBr$_3$ to have a wide PL emission temperature range of up to 393 K and 454 K. More importantly, the PL quenching intimately linked to structural phase transitions also indicates that (TECA)PbBr$_3$ and (TEBA)PbBr$_3$ are valuable bistable switching materials. This study not only expands the repertoire of OIMH photoluminescent phase transition materials but also paves the way for exploring multifunctional OIMHs and their the pivotal structure–property relationship.

2296 | *Inorg. Chem. Front.*, 2024, **11**, 2290–2299

This journal is © the Partner Organisations 2024

Experimental

Materials

Triethylamine (Macklin, 98%), *N*,*N*-diethyl-*N*-methyl-ethanaminium bromide (TEMA·Br) (Aladdin, 99%), bromo-chloromethane (Aladdin, 98%), 1, 2-dibromomethane (Macklin, 98%), lead(II) bromide (Macklin, 98%), and hydrogen bromide (Sinopharm, 36–38%) were used. All chemicals and reagents were purchased directly from the chemical reagent company and used directly without further purification.

Synthesis

Triethylbromomethylammonium bromide (TEBA)·Br was synthesized according to the following steps. Firstly, approximately 100 mL of acetonitrile was added to a 250 mL round bottom flask, triethylamine (200 mmol, 20.238 g) was slowly added to it at room temperature, then 1,2-dibromomethane (200 mmol, 34.766 g) was added, stirred well, and refluxed at 328 K for 48 hours. Most of the solvent was evaporated using a rotary evaporator, followed by rinsing three times with ethyl acetate, and filtering to obtain a white powder product. Similarly, 1,2-dibromomethane was replaced with bromochloromethane (200 mmol, 25.876 g) and reacted under the same conditions to obtain triethylchloromethylammonium bromide (TECA)·Br.

(TEMA)PbBr$_3$, (TECA)PbBr$_3$ and (TEBA)PbBr$_3$

An experimental procedure was conducted to synthesize rod-shaped crystals from (TEMA)·Br and PbBr$_2$. Firstly, (TEMA)·Br (1.880 mg, 2 mmol) was weighed and dissolved in a hydrobromic acid solution (99%) in a 25 ml beaker. The solution was stirred thoroughly. PbBr$_2$ (1.854 g, 5.0 mmol) was added under stirring conditions, and HBr solution was gradually added dropwise until the solution became clear. The solution was then evaporated on a 328 K hot plate. After 4 days, colorless transparent rod-shaped crystals were formed. The synthesis methods of (TECA)PbBr$_3$ and (TEBA)PbBr$_3$ are similar to that for (TEMA)PbBr$_3$, except that (TEMA)·Br was replaced by (TECA)·Br and (TEBA)·Br. In addition, the phase purity and structural composition of the target crystal samples were determined using PXRD and the infrared (IR) spectra (Fig. S3 and S4†).

Author contributions

Z.-J. W. performed the experiments, data analysis, and wrote the manuscript. M.-J. S., Z.-P. R. and P.-Z. H. assisted in the auxiliary analysis of the data and revised the manuscript. DFT calculations were performed by M.-M. L and J.-Y. L., D.-W. F, and H.-F. L. Y. Z. guided and supervised this work. All the authors reviewed the manuscript.

Conflicts of interest

The authors declare no conflict of interest.

Acknowledgements

References

1 M. Li and Z. Xia, Recent progress of zero-dimensional luminescent metal halides, *Chem. Soc. Rev.*, 2021, **50**, 2626–2662.

2 L. N. Quan, B. P. Rand, R. H. Friend, S. G. Mhaisalkar, T.-W. Lee and E. H. Sargent, Perovskites for next-generation optical sources, *Chem. Rev.*, 2019, **119**, 7444–7477.

3 T. Zhang, K. Xu, J. Li, L. He, D.-W. Fu, Q. Ye and R.-G. Xiong, Ferroelectric hybrid organic–inorganic perovskites and their structural and functional diversity, *Natl. Sci. Rev.*, 2023, **10**, nwac240.

4 L. Zhang, S. Li, H. Sun, Y. Fang, Y. Wang, K. Wang, H. Jiang, L. Sui, G. Wu, K. Yuan and B. Zou, Manipulating lone-pair-driven luminescence in 0D tin halides by pressure-tuned stereochemical activity from static to dynamic, *Angew. Chem., Int. Ed.*, 2023, **62**, e202311912.

5 H. Fattal, T. D. Creason, C. J. Delzer, A. Yangui, J. P. Hayward, B. J. Ross, M.-H. Du, D. T. Glatzhofer and B. Saparov, Zero-dimensional hybrid organic–inorganic indium bromide with blue emission, *Inorg. Chem.*, 2021, **60**, 1045–1054.

6 B. Li, J. Jin, M. Yin, X. Zhang, M. S. Molokeev, Z. Xia and Y. Xu, Sequential and reversible phase transformations in zero-dimensional organic–inorganic hybrid sb-based halides towards multiple emissions, *Angew. Chem., Int. Ed.*, 2022, **61**, e202212741.

7 K. Liu, S. Hao, J. Cao, J. Lin, L. Fan, X. Zhang, Z. Guo, C. Wolverton, J. Zhao and Q. Liu, Antimony doping to enhance luminescence of tin(IV)-based hybrid metal halides, *Inorg. Chem. Front.*, 2022, **9**, 3865–3873.

8 M. Mączka, D. Drozdowski, D. Stefańska and A. Gągor, Zero-dimensional mixed-cation hybrid lead halides with broadband emissions, *Inorg. Chem. Front.*, 2023, **10**, 7222–7230.

9 T. Li, T. Huang, Q. Wei, W. Lin, X. Lu, X. Shen, S. Zhou, W. Liang and B. Zou, Mixed B-site driven [InBr$_4$]$^-$ tetrahedral efficient blue emission, *Chem. Eng. J.*, 2023, **477**, 146872.

10 L. Zhang, S. Li, H. Sun, Q. Jiang, Y. Wang, Y. Fang, Y. Shi, D. Duan, K. Wang, H. Jiang, L. Sui, G. Wu, K. Yuan and B. Zou, Revealing the mechanism of pressure-induced

This journal is © the Partner Organisations 2024

Inorg. Chem. Front., 2024, **11**, 2290–2299 | **2297**

emission in layered silver–bismuth double perovskites, *Angew. Chem., Int. Ed.*, 2023, **62**, e202301573.

11 Q. Ren, J. Zhang, M. S. Molokeev, G. Zhou and X.-M. Zhang, Triplet–triplet energy transfer from Bi^{3+} to Sb^{3+} in zero-dimensional indium hybrids via a B-site co-doping strategy toward white-light emission, *Inorg. Chem. Front.*, 2022, **9**, 5960–5968.

12 Y. Wu, C.-M. Shi, S.-R. Kang and L.-J. Xu, Antimony-doped indium-based halide single crystals enabling white-light emission, *Inorg. Chem. Front.*, 2022, **9**, 5008–5015.

13 G. Zhou, Z. Liu, M. S. Molokeev, Z. Xiao, Z. Xia and X.-M. Zhang, Manipulation of Cl/Br transmutation in zero-dimensional Mn^{2+}-based metal halides toward tunable photoluminescence and thermal quenching behaviors, *J. Mater. Chem. C*, 2021, **9**, 2047–2053.

14 M. Li, J. Zhou, G. Zhou, M. S. Molokeev, J. Zhao, V. Morad, M. V. Kovalenko and Z. Xia, Hybrid metal halides with multiple photoluminescence centers, *Angew. Chem., Int. Ed.*, 2019, **58**, 18670–18675.

15 X. Zhao, M. Wu, H. Liu, Y. Wang, K. Wang, X. Yang and B. Zou, Pressure-treated engineering to harvest enhanced green emission in mn-based organic–inorganic metal halides at ambient conditions, *Adv. Funct. Mater.*, 2022, **32**, 2109277.

16 L. Zhou, J.-F. Liao, Z.-G. Huang, J.-H. Wei, X.-D. Wang, H.-Y. Chen and D.-B. Kuang, Intrinsic self-trapped emission in 0D lead-free $(C_4H_{14}N_2)_2In_2Br_{10}$ single crystal, *Angew. Chem., Int. Ed.*, 2019, **58**, 15435–15440.

17 L.-K. Wu, R.-F. Li, W.-Y. Wen, Q.-H. Zou, H.-Y. Ye and J.-R. Li, Lead-free hybrid indium perovskites with near-unity PLQY and white light emission using an Sb^{3+} doping strategy, *Inorg. Chem. Front.*, 2023, **10**, 3297–3306.

18 G. Zhang, C. Yang, Q. Wei, J. Long, X. Shen, Y. Chen, B. Ke, W. Liang, X. Zhong and B. Zou, Sb^{3+}-doped indium-based metal halide $(Gua)_3InCl_6$ with efficient yellow emission, *ACS Appl. Mater. Interfaces*, 2024, **16**, 3841–3852.

19 B. Su, G. Zhou, J. Huang, E. Song, A. Nag and Z. Xia, Mn^{2+}-doped metal halide perovskites: Structure, photoluminescence, and application, *Laser Photonics Rev.*, 2021, **15**, 2000334.

20 Y. Wang, T. Zhang, M.-M. Lun, F.-L. Zhou, D.-W. Fu and Y. Zhang, Halogen regulation triggers NLO and dielectric dual switches in hybrid compounds with green fluorescence, *Inorg. Chem. Front.*, 2021, **8**, 4230–4238.

21 T. Zhang, J.-Y. Li, G.-W. Du, K. Ding, X.-G. Chen, Y. Zhang and D.-W. Fu, Thermally-driven unusual dual SHG switching with wide SHG-active steps triggered by inverse symmetry breaking, *Inorg. Chem. Front.*, 2022, **9**, 4341–4349.

22 X.-N. Hua, W.-Q. Liao, Y.-Y. Tang, P.-F. Li, P.-P. Shi, D. Zhao and R.-G. Xiong, A room-temperature hybrid lead iodide perovskite ferroelectric, *J. Am. Chem. Soc.*, 2018, **140**, 12296–12302.

23 Z. Wei, W.-Q. Liao, Y.-Y. Tang, P.-F. Li, P.-P. Shi, H. Cai and R.-G. Xiong, Discovery of an antiperovskite ferroelectric in $[(CH_3)_3NH]_3(MnBr_3)(MnBr_4)$, *J. Am. Chem. Soc.*, 2018, **140**, 8110–8113.

24 W.-Y. Zhang, Y.-Y. Tang, P.-F. Li, P.-P. Shi, W.-Q. Liao, D.-W. Fu, H.-Y. Ye, Y. Zhang and R.-G. Xiong, Precise molecular design of high-T_{rc} 3D organic–inorganic perovskite ferroelectric: [MeHdabco]RbI₃ (MeHdabco = *N*-methyl-1,4-diazoniabicyclo[2.2.2]octane), *J. Am. Chem. Soc.*, 2017, **139**, 10897–10902.

25 H.-Y. Zhang, X.-G. Chen, Z.-X. Zhang, X.-J. Song, T. Zhang, Q. Pan, Y. Zhang and R.-G. Xiong, Methylphosphonium tin bromide: A 3D perovskite molecular ferroelectric semiconductor, *Adv. Mater.*, 2020, **32**, 2005213.

26 X.-G. Chen, X.-J. Song, Z.-X. Zhang, P.-F. Li, J.-Z. Ge, Y.-Y. Tang, J.-X. Gao, W.-Y. Zhang, D.-W. Fu, Y.-M. You and R.-G. Xiong, Two-dimensional layered perovskite ferroelectric with giant piezoelectric voltage coefficient, *J. Am. Chem. Soc.*, 2020, **142**, 1077–1082.

27 Y. Zhang, X.-J. Song, Z.-X. Zhang, D.-W. Fu and R.-G. Xiong, Piezoelectric energy harvesting based on multiaxial ferroelectrics by precise molecular design, *Matter*, 2020, **2**, 697–710.

28 J.-Q. Wang, G. Teri, H.-F. Ni, Q.-F. Luo, X.-P. Wang, D.-W. Fu, Y. Zhang and Q. Guo, Halogenation triggering rules in hybrid materials for fluorescence and dielectric phase transitions, *Inorg. Chem. Front.*, 2023, **10**, 3860–3866.

29 H.-F. Ni, J.-H. Lin, C.-F. Wang, Q.-F. Luo, P.-Z. Huang, Z.-X. Zhang, D.-W. Fu and Y. Zhang, Molecular orientation dynamics triggers ferroelectricity and ferroelasticity in an organic–inorganic halide material, *Inorg. Chem. Front.*, 2023, **10**, 7231–7237.

30 D.-W. Fu, J.-X. Gao, W.-H. He, X.-Q. Huang, Y.-H. Liu and Y. Ai, High-T_c enantiomeric ferroelectrics based on homo-chiral Dabco-derivatives (Dabco=1,4-diazabicyclo[2.2.2]octane), *Angew. Chem., Int. Ed.*, 2020, **59**, 17477–17481.

31 Q. Jia, T. Shao, L. Tong, C. Su, D. Fu and H. Lu, Lead-free bilayer heterometallic halide perovskite with reversible phase transition and photoluminescence properties, *Chin. Chem. Lett.*, 2023, **34**, 107539.

32 J.-X. Gao, W.-Y. Zhang, Z.-G. Wu, Y.-X. Zheng and D.-W. Fu, Enantiomorphic perovskite ferroelectrics with circularly polarized luminescence, *J. Am. Chem. Soc.*, 2020, **142**, 4756–4761.

33 X.-J. Song, T. Zhang, Z.-X. Gu, Z.-X. Zhang, D.-W. Fu, X.-G. Chen, H.-Y. Zhang and R.-G. Xiong, Record enhancement of Curie temperature in host–guest inclusion ferroelectrics, *J. Am. Chem. Soc.*, 2021, **143**, 5091–5098.

34 D.-W. Fu, J.-X. Gao, P.-Z. Huang, R.-Y. Ren, T. Shao, L.-J. Han, J. Liu and J.-M. Gong, Observation of transition from ferroelasticity to ferroelectricity by solvent selective effect in anilinium bromide, *Angew. Chem., Int. Ed.*, 2021, **60**, 8198–8202.

35 Y. Xie, Y. Ai, Y.-L. Zeng, W.-H. He, X.-Q. Huang, D.-W. Fu, J.-X. Gao, X.-G. Chen and Y.-Y. Tang, The soft molecular polycrystalline ferroelectric realized by the fluorination effect, *J. Am. Chem. Soc.*, 2020, **142**, 12486–12492.

36 K. Ding, H. Ye, C. Su, Y.-A. Xiong, G. Du, Y.-M. You, Z.-X. Zhang, S. Dong, Y. Zhang and D.-W. Fu, Superior ferroelectricity and nonlinear optical response in a hybrid ger-

2298 | *Inorg. Chem. Front.*, 2024, **11**, 2290–2299

This journal is © the Partner Organisations 2024

manium iodide hexagonal perovskite, *Nat. Commun.*, 2023, **14**, 2863.

37 J.-Y. Li, T. Zhang, M.-M. Lun, Y. Zhang, L.-Z. Chen and D.-W. Fu, Facile control of ferroelectricity driven by ingenious interaction engineering, *Small*, 2023, **19**, 2301364.

38 Y.-Y. Zhang, J.-Q. Luo, Y. Han, W.-Y. Zhang, Y. Zhang, H.-F. Lu and D.-W. Fu, Bistable switch molecule DPACdCl$_4$ showing four physical channels and high phase transition temperature, *Chin. Chem. Lett.*, 2024, DOI: **10.1016/j.cclet.2024.109530**.

39 L.-P. Miao, N. Ding, N. Wang, C. Shi, H.-Y. Ye, L. Li, Y.-F. Yao, S. Dong and Y. Zhang, Direct observation of geometric and sliding ferroelectricity in an amphidynamic crystal, *Nat. Mater.*, 2022, **21**, 1158–1164.

40 X.-T. Sun, H.-F. Ni, Y. Zhang and D.-W. Fu, Hybrid perovskite shows temperature-dependent PL and dielectric response triggered by halogen substitution, *Chin. J. Struct. Chem.*, 2023, DOI: **10.1016/j.cjsc.2023.100212**.

41 Y.-Z. Zhang, D.-S. Sun, X.-G. Chen, J.-X. Gao, X.-N. Hua and W.-Q. Liao, Optical-dielectric duple bistable switches: Photoluminescence of reversible phase transition molecular material, *Chem. – Asian J.*, 2019, **14**, 3863–3867.

42 Q. Guo, W.-Y. Zhang, C. Chen, Q. Ye and D.-W. Fu, Redlight emission and dielectric reversible duple opto-electronic switches in a hybrid multifunctional material: (2-Methylimidazolium)MnCl$_3$(H$_2$O), *J. Mater. Chem. C*, 2017, **5**, 5458–5464.

43 F.-J. Geng, D.-H. Wu, L. Zhou, P.-P. Shi, P.-F. Li, J.-X. Gao, X. Zheng, D.-W. Fu and Q. Ye, Photoluminescent-dielectric duple switch in a perovskite-type high-temperature phase transition compound: [(CH$_3$)$_3$PCH$_2$OCH$_3$][PbBr$_3$], *Dalton Trans.*, 2017, **46**, 9528–9534.

44 M.-M. Lun, H.-F. Ni, Z.-X. Zhang, J.-Y. Li, Q.-Q. Jia, Y. Zhang, Y. Zhang and D.-W. Fu, Unusual thermal quenching of photoluminescence from an organic–inorganic hybrid [MnBr$_4$]$^{2-}$-based halide mediated by crystalline–

crystalline phase transition, *Angew. Chem., Int. Ed.*, 2024, **63**, e202313590.

45 I. Spanopoulos, I. Hadar, W. Ke, P. Guo, S. Sidhik, M. Kepenekian, J. Even, A. D. Mohite, R. D. Schaller and M. G. Kanatzidis, Water-Stable 1D hybrid tin(II) iodide emits broad light with 36% photoluminescence quantum efficiency, *J. Am. Chem. Soc.*, 2020, **142**, 9028–9038.

46 G. Cavallo, P. Metrangolo, R. Milani, T. Pilati, A. Priimagi, G. Resnati and G. Terraneo, The halogen bond, *Chem. Rev.*, 2016, **116**, 2478–2601.

47 Z. Cai, X. Zhang, S. Xiao, S. Ge, X. Liu, Y. Zhang, L. Chen, X.-N. Hua and B. Sun, Design, synthesis, and characterization of a new hybrid organic–inorganic perovskite with a high-T_c dielectric transition, *Dalton Trans.*, 2023, **52**, 955–961.

48 Z.-J. Wang, H.-F. Ni, T. Zhang, J. Li, M.-M. Lun, D.-W. Fu, Z.-X. Zhang and Y. Zhang, Targeted regulation and optimization of multifunctional phase transition materials by novel void occupancy engineering, *Chem. Sci.*, 2023, **14**, 9041–9047.

49 K. Robinson, G. V. Gibbs and P. H. Ribbe, Quadratic elongation: A quantitative measure of distortion in coordination polyhedra, *Science*, 1971, **172**, 567–570.

50 M.-M. Lun, F.-L. Zhou, D.-W. Fu and Q. Ye, Multi-functional hybrid perovskites with triple-channel switches and optical properties, *J. Mater. Chem. C*, 2022, **10**, 11371–11378.

51 L. Mao, P. Guo, M. Kepenekian, I. Hadar, C. Katan, J. Even, R. D. Schaller, C. C. Stoumpos and M. G. Kanatzidis, Structural diversity in white-light-emitting hybrid lead bromide perovskites, *J. Am. Chem. Soc.*, 2018, **140**, 13078–13088.

52 C. Xue, H. Huang, S. Nishihara, V. Biju, X.-M. Ren and T. Nakamura, Inorganic chain mediated excitonic properties in one-dimensional lead halide hybrid perovskites, *J. Phys. Chem. Lett.*, 2022, **13**, 7405–7412.

This journal is © the Partner Organisations 2024

Inorg. Chem. Front., 2024, **11**, 2290–2299 | **2299**